Fundamental noise characterization of a ducted propeller in hover

Frank Simon[1]
DMPE - ONERA - Université de Toulouse
F-31055, Toulouse, France

Noah H. Schiller[2], Nikolas S. Zawodny[3], Nicole A. Pettingill[4], Matthew B. Galles[5]
NASA Langley Research Center
Hampton, Virginia 23681, USA

ABSTRACT

Unmanned aerial vehicles (UAVs) are currently being used for reconnaissance missions, tactical surveillance, and infrastructure inspection. When legislation allows it, these devices will provide additional services close to inhabited areas, which could lead to noise complaints. On most UAVs, the propellers are the dominant source of noise. As a result, researchers have studied the impact of propeller shape and blade count on noise. Much of this work, however, has focused on isolated propellers. While different UAV concepts are equipped with ducts for aerodynamic and protection reasons, few studies focus on the acoustic benefit of ducts, as is achieved, for example, on turbofan aircraft. The objectives of this paper are: first, to simulate the noise radiation of a UAV propeller in static conditions based on its location in a hard wall duct; second, to analyze the contribution of the different acoustic source components (i.e., thrust, torque, and thickness); and third, to validate the approach with experiments conducted in the NASA Small Hover Anechoic Chamber over a range of propeller rotation rates. For the propeller and duct geometries considered in this experiment, it is shown that the best attenuation is achieved when the propeller is centered axially in the duct because of interference between upstream and downstream radiated waves.

1. INTRODUCTION

Unmanned aerial vehicles (UAVs) are being developed for various applications including reconnaissance, tactical surveillance, infrastructure inspection (e.g., bridges, buildings, and rail networks), and even inventory management in distribution centers. In the future, UAVs could also be used to provide personal services (e.g., delivery and even personal transportation) in populated areas. All of these applications would benefit from quieter vehicles.

While many UAVs have electric motors that may generate high frequency tonal noise, propellers are typically the dominant noise source producing both tonal and broadband noise [1, 2]. Researchers have therefore considered various strategies to reduce propeller noise including varying the blade shape, propeller airframe spacing, propeller layout, and blade surface texture [3-8]. Ducts can also be used around the propellers to modify the acoustic radiation. For example, Martin and Boxwell [9] measured the noise radiated by a 2-bladed propeller surrounded by a 25.4 cm diameter rigid duct. The acoustic test, conducted in hover-type conditions, showed that the duct can increase the broadband noise relative to an isolated propeller if the duct leading edge radius is too small. The duct, however, was found to have little impact on the tonal noise at the blade passage frequency (BPF). In contrast, Malgoezar et al. [10] tested a 30 cm diameter duct in an anechoic wind tunnel and found

that the duct reduced the tonal noise at the BPF relative to an isolated propeller, particularly with low-speed (i.e., 10 m/s) background flow. The background flow also reduced the broadband noise of the ducted propeller relative to the no-flow test.

The purpose of this study is to provide a fundamental numerical assessment of the impact of the duct on acoustic propagation and scattering at the propeller BPF. The objectives of the paper are: first, to simulate the tonal noise at the BPF for a ducted propeller in hover conditions; second, to analyze the contribution of different tonal source components (steady loading and thickness noise); and third, to compare predictions with experiments conducted in an anechoic chamber with low-speed background flow.

2. THEORETICAL "RING SOURCE" APPROACH

To assess the effect of a duct on acoustic radiation at the propeller BPF, this study relies on a propeller noise formulation implemented in an acoustic finite element model. The formulation captures steady loading and thickness noise radiated from an isolated propeller but does not account for changes in the flow characteristics or loading conditions due to the duct. Instead, the blade shape, operating conditions, thrust, and torque are all inputs to the model.

Asymptotic approximations can be used to understand the 3D structure of the pressure field produced by a spinning sinusoidal distribution of steady loading and thickness sources. These formulations highlight the presence of creeping evanescent waves in the near field that do not radiate efficiently to the far-field, but still interact with the duct [11,12]. These types of formulations often provide directivity but not absolute source pressure, which depends on the loading and design of the propeller.

The formulation by Garrick and Watkins [13], describing near-field pressure as a function of thrust and torque, is used in this study. Specifically, the effective ring approximation is used, which assumes the thrust T and torque Q are concentrated on an annular ring instead of distributed over the propeller disk. The annular ring is placed at an effective propeller radius r_e, usually 0.8 of the blade radius, as depicted in Figure 1 (a). The pressure field due to the thrust and torque components can be defined as:

$$p_T = \mp \frac{1}{2\pi} \int_0^{2\pi} \frac{T e^{imB\varphi}}{r_e} \frac{\partial G(\mathrm{R}, r_e)}{\partial z} r_e \, d\varphi \tag{1}$$

and

$$p_Q = \frac{1}{2\pi} \int_0^{2\pi} imB \frac{Q e^{imB\varphi}}{r_e^3} G(\mathrm{R}, r_e) r_e \, d\varphi \tag{2}$$

where m is the harmonic number, B is the blade count, φ is the azimuthal angle, $G(\mathrm{R}, r_e) = e^{-ikR}/4\pi R$ is the free-space Green's function with R defined as the distance between the observer and an elemental radiator on the annular ring, k is the acoustic wavenumber, and z is the propeller axis.
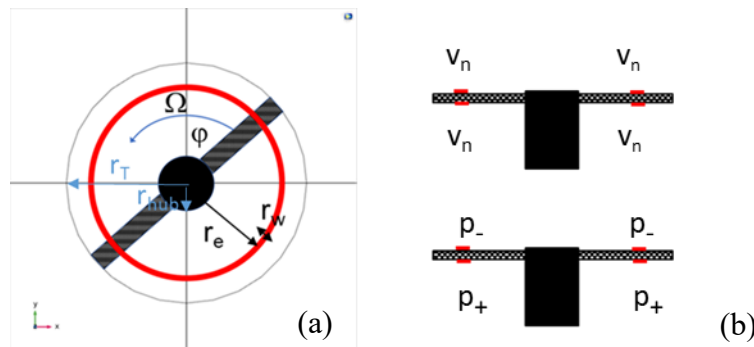

Figure 1: (a) Top view of a notional propeller with the effective annular ring in red and (b) the distribution of torque and thrust sources on a cross section of the propeller disk.

For modeling purposes, it is useful to define equivalent sources on the top and bottom surfaces of the annular ring. The thrust component is modeled by specifying the surface pressure p at each point on the ring as:

$$p_{\mp} = \mp \frac{T e^{imB\varphi}}{2\pi r_e r_w} \tag{3}$$

where r_w is the width of the annular ring. The thrust component is equivalent to a rotating dipole and therefore the pressure on the top and bottom surfaces of the ring are out of phase, as depicted in Figure 1 (b). In contrast the torque component is equivalent to a rotating monopole and therefore has the same phase on both the top and bottom surfaces of the ring. The torque component is modeled using a normal velocity source v_n defined on the top and bottom surfaces of the ring as:

$$v_n = \frac{Q m B e^{imB\varphi}}{4\rho\pi^2 r_e^3 r_w f} \tag{4}$$

where f is frequency and ρ is the density of air.

The formulation by Hanson [14, 15], in terms of the Fourier transform of the chordwise thickness, is used to define the source pressure on the propeller disk as:

$$p_{tn} = -\frac{\rho B \omega^2 b^2 t_b}{\pi} \int_A e^{imB\varphi} \frac{1}{r} G(\mathrm{R}, r) \left\{ \int_{-1/2}^{1/2} H(X) e^{ik_x X} dX \right\} dA \tag{5}$$

where b is the airfoil chord length, t_b is the ratio of the airfoil thickness to the chord length, $G(\mathrm{R}, r) = e^{-ikR}/4\pi R$ is the free-space Green's function with R defined as the distance between the observer and an elemental radiator on the propeller disk, and $H(X)$ is the normalized thickness distribution as depicted in Figure 2 for an NACA 0012 with X as the normalized chordwise coordinate. In this case, the equivalent sources are not concentrated at an effective radius but are instead distributed over the propeller disk and depicted in Figure 3 (a).
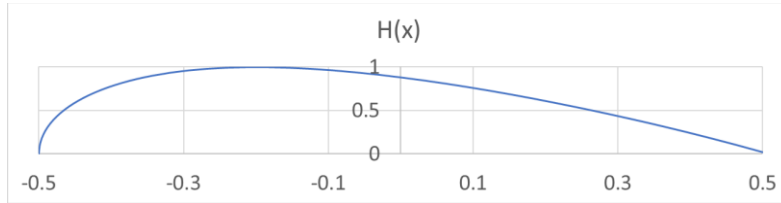

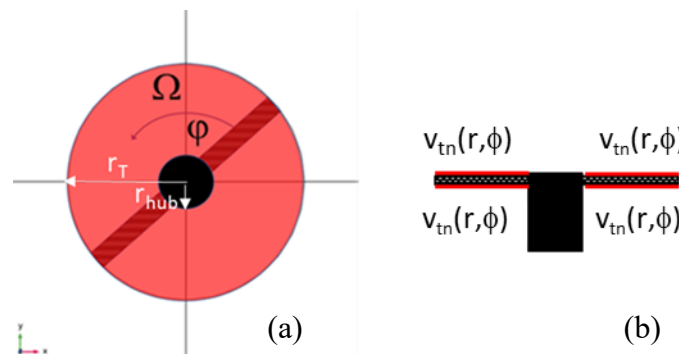Figure 2: Normalized thickness distribution for an NACA 0012 airfoil.

Figure 3: (a) Propeller ring and (b) thickness distribution normal to the propeller ring.

For modeling purposes, equivalent sources are defined on the top and bottom surfaces of the propeller disk to capture thickness noise. This type of noise is generated by a rotating volume displacement or velocity like a rotating monopole, and is therefore modeled using a normal velocity source defined on the top and bottom surfaces of the propeller disk:

$$v_{tn} = iBf b^2 t_b e^{imB\varphi} \frac{1}{r} h_{mB}(r) \tag{6}$$

with the Fourier transform of the chordwise distribution h_{mB} defined as:

$$h_{mB}(r) = \int_{-1/2}^{1/2} H(X) e^{-imBbX/r} dX \tag{7}$$

Note that the velocity on the top and bottom surfaces of the propeller disk are in phase for this type of source, as depicted in Figure 3 (b).

Inputs to the model include the propeller geometry, the rotation rate, as well as propeller thrust and torque. For this study, the thrust and torque were either obtained from blade element momentum theory code or measured results. It is important to note that the presence of the duct can change the flow characteristics and modify the loading on the blades, which in turn will change the thrust and torque. The blade element momentum theory predictions did not capture the effect of the duct, but the measured results for the ducted configurations do capture the change in loading.

3. NUMERICAL PREDICTIONS

Acoustic propagation and scattering are captured using an acoustic finite element model developed in COMSOL Multiphysics®. As described in the previous section, the propeller is represented as a disk, with the source components due to thrust and torque concentrated on an annular ring, as highlighted on the right in Figure 4, and the thickness component distributed over the surface of the propeller disk. Each noise source is modeled separately, and then the resulting pressure fields are combined to determine the total pressure field for all three components. A simple canonical duct is also included in the model. All surfaces of the duct are assumed rigid, and the assembly (consisting of the propeller disk and duct) is embedded in a large acoustic domain terminated by a perfectly matched layer to approximate free-field conditions. The model is solved in the frequency domain at the propeller BPF.

The propeller considered in this study has three blades with a diameter of 24.4 cm. The blades have no twist or sweep and have an airfoil shape based on an NACA 0012, which is symmetric with no camber and a maximum thickness that is 12% of the chord length. The chord length of the blades is 2.1 cm and the blades have a constant pitch of 10 degrees. The nominal rotation rate of the propeller is 9000 RPM and the assumed thrust and torque are 8.38 N and 0.12 Nm, respectively. In this case, thrust and torque were estimated using the Propeller Analysis System (PAS) module [16] within the Aircraft Noise Prediction Program (ANOPP) [17].

The duct has a 25.4 cm inner diameter (D) with straight walls that are 3.0 cm thick (t). The outer mold line is symmetric, as depicted in Figure 4, with leading and trailing edge radii (r_{LE}) of 1.5 cm. Two different duct chord lengths (c) are considered, a longer 15 cm duct and a shorter 9.1 cm duct. The relevant duct dimensions are summarized in Table 1.
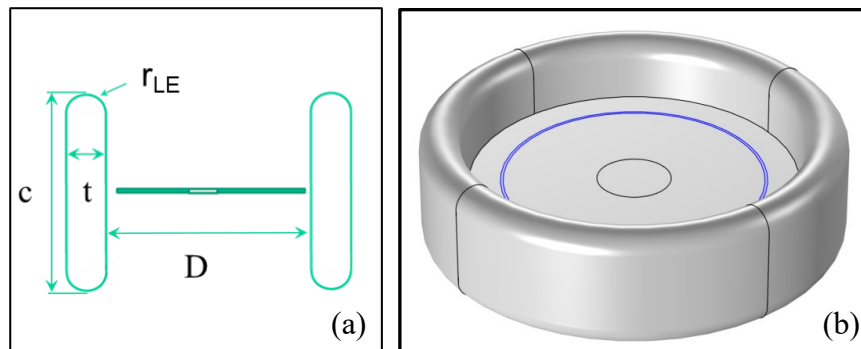

Figure 4: (a) Cross-section of the duct and (b) isometric view of the propeller disk in the duct with the annular ring in blue (right).

Table 1: Duct characteristics.

D (cm)	c (cm)	t (cm)	r_{LE} (cm)
25.4	15 or 9.1	3.0	1.5

Figure 5 shows the torque, thrust, and thickness pressure fields for the isolated and ducted propellers at the BPF. There are six sound pressure level contour plots shown. The left half of each contour plot shows the isolated propeller configuration, and the right half of each plot shows the ducted configuration. Presenting the pressure fields in this manner allows for a visual comparison between the two hemispheres. The figures on the top correspond to the configuration with the propeller close to the duct inlet, while the figures on the bottom show predictions with the propeller centered axially in the duct. In this case, the duct length is short relative to the acoustic wavelength (i.e., $c \approx \lambda/5$ where λ is the acoustic wavelength at the BPF). Radiation from the inlet and exhaust interact generating different interference patterns based on the location of the propeller in the duct. Radiated sound power, calculated by integrating acoustic intensity on a sphere surrounding the system, is shown below each figure. Values in black correspond to the isolated propeller and values in red correspond to the ducted configuration. Regardless of the axial location of the propeller, the presence of the duct reduces the radiated sound power for both the torque and thickness sources. The change in sound power is attributed to a change in the radiation efficiency of the ducted sources. The same trend does not hold for thrust. When the propeller is positioned near the inlet, the asymmetry of the configuration increases the radiated power of the thrust source relative to the isolated propeller. When the propeller is centered in the duct, however, the radiated power of the thrust source is reduced by 5.6 dB.
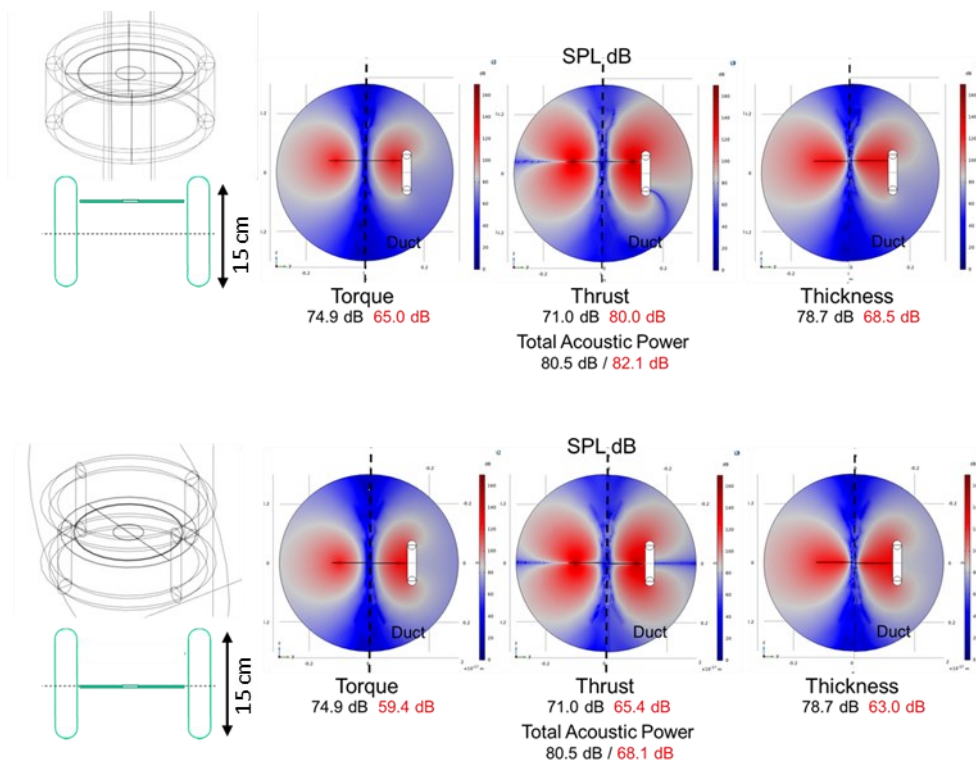

Figure 5: Torque, thrust, and thickness sound pressure level contours for isolated (left half of each subfigure) and ducted propellers (right half of each subfigure) at different axial positions. The labels below each contour show radiated sound power for the isolated (black) and ducted (red) configurations.

Figure 6 shows predictions for the shorter duct. In this case, the duct does not significantly affect the radiated power for the thrust component, however, it does reduce thickness and torque noise.
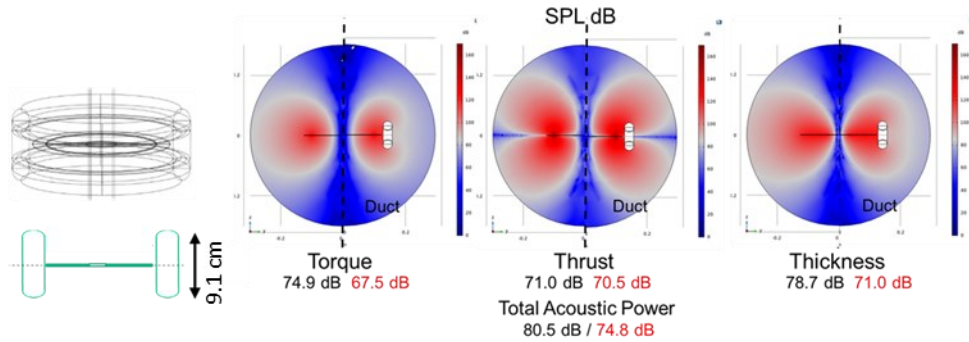
Figure 6: Torque, thrust, and thickness sound pressure level contours for the isolated propeller (left half of each subfigure) and short ducted propeller (right half of each subfigure). The labels below each contour show radiated sound power for the isolated (black) and ducted (red) configurations.

Figure 7 compares the radiated sound power for the isolated propeller and the ducted configurations with the propeller centered axially in the duct. The biggest reductions are achieved in torque and thickness noise, which radiate most efficiently in the plane of the propeller. The reduction in thrust noise is more modest, particularly for the short duct. Overall, the short duct reduces the combined radiated sound power at the BPF by close to 6 dB while the longer duct reduces the radiated power by over 12 dB. Note that while thickness noise is dominant for the isolated configuration, thrust noise becomes equally important for the ducted configurations.
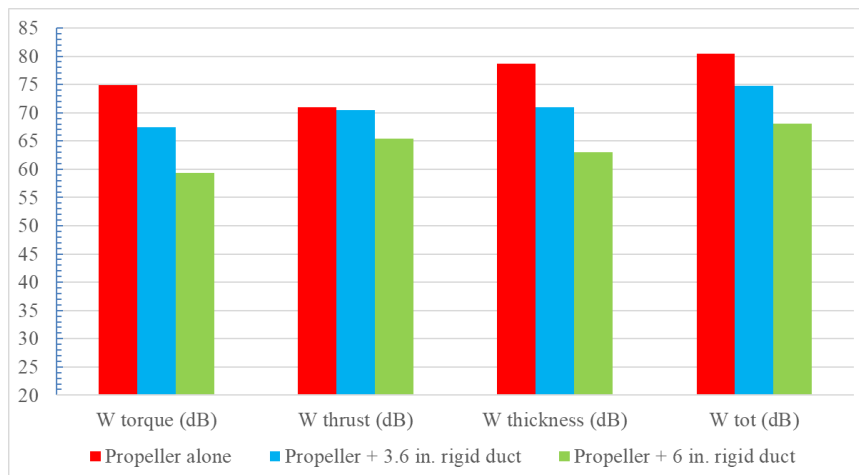

Figure 7: Torque, thrust, thickness, and total radiated sound power (dB) for isolated and ducted propellers.

3. EXPERIMENTAL SETUP

The propeller and 9.1 cm long duct described in the previous section were 3D printed from a hard acrylate-based plastic and tested in the Small Hover Anechoic Chamber (SHAC) at the NASA Langley Research Center. The anechoic chamber is 3.87 m by 2.56 m by 3.26 m from wedge tip to wedge tip and is acoustically treated to provide a nearly anechoic environment down to 250 Hz. The facility has an inlet and exhaust fan capable of low-speed background flow at approximately 5 m/s. All tests reported in this paper were conducted with 5 m/s background flow in the axial direction to improve the flow quality through the duct and reduce the flow separation from the inlet lip of the duct. Mesh screens are typically installed downstream of the propeller to delay the onset of flow recirculation in this facility. However, the screens were not necessary with background flow and were therefore removed for this test.

A laser tachometer was used to measure the rotation rate of the propeller, and separate load cells connected to the propeller and duct provided aerodynamic loads. An eight-element microphone array, depicted in Figure 8, was used for acoustic measurements. The microphones are all in the acoustic

far-field and span a range of elevation angles from +37.3 degrees above the propeller plane to -50.1 degrees below the propeller plane.
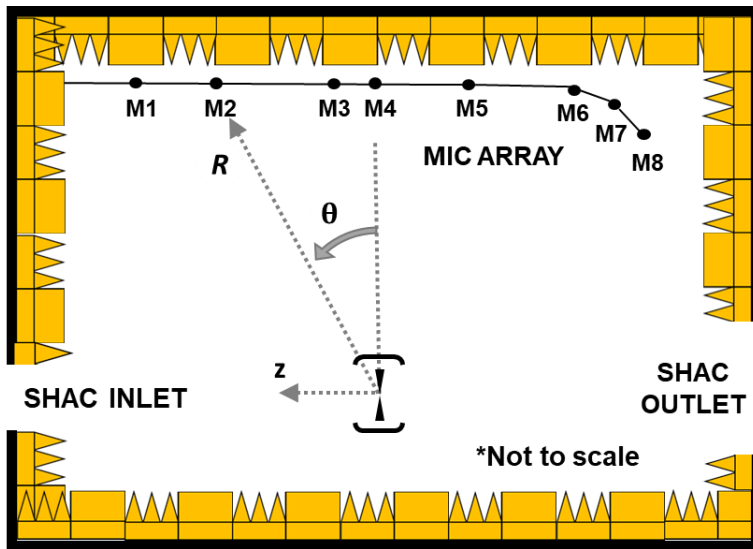
Mic #	R (cm)	θ (deg)
1	238	37.3
2	210	25.8
3	194	5.7
4	191	-0.8
5	204	-19.2
6	230	-35.2
7	231	-43.5
8	223	-50.1

Figure 8: Microphone layout in the Small Hover Anechoic Chamber. Flow is in the negative z direction.

Three different configurations were tested: an isolated propeller; a ducted propeller with the propeller positioned 2.5 cm upstream of the duct center; and a ducted propeller with the propeller centered axially in the duct. Each configuration was tested with nominal propeller rotation rates of 8000, 8400, and 9000 RPM. Following the test, the acoustic data were converted to the frequency domain and the tonal level at the BPF was extracted by summing the energy within $\pm$ 3 Hz of the spectral peak.

4. RESULTS

4.1 Isolated Propeller

Table 2 shows the measured thrust and torque for the isolated propeller at each rotation rate. The measured rotational speed, thrust, and torque were subsequently used as inputs to the acoustic model. Predictions of the sound pressure level with the updated inputs at the BPF for the isolated propeller are shown in Figure 9 (a). Corresponding measurements are included in Figure 9 (b). The general trends are similar in both figures with higher levels in the propeller plane (around microphones 3 and 4) and roll off in the upstream and downstream directions toward microphones 1 and 8, respectively. While the microphones are not equidistant from the source, corrections accounting for the propagation distance change the levels by less than 2 dB and do not change the overall trend. As expected, the thrust, torque, and acoustic levels all increase with RPM. While the predictions shown in Figure 9 (a) capture these trends, the levels are lower than the measurements by approximately 3 dB.

Table 2: Measured propeller thrust and torque for the isolated propeller.

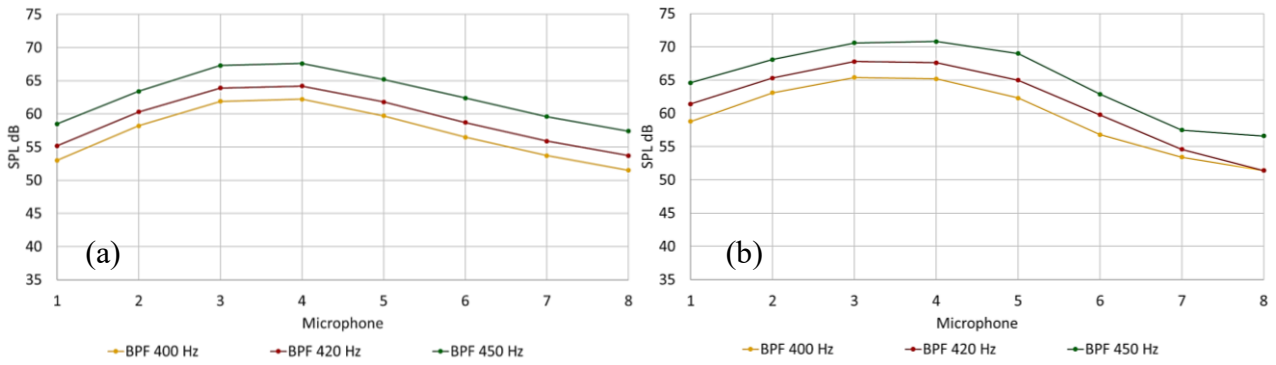| RPM	BPF (Hz)	Thrust (N)	Torque (Nm)
8010	400	4.27	0.08
8408	420	4.81	0.09
9040	452	5.76	0.11

Figure 9: (a) Predicted and (b) measured sound pressure level (dB re. 20 µPa) at the BPF for the isolated propeller at three different rotation rates.

4.2 Ducted Propeller

Tables 3 and 4 contain the measured thrust and torque with the propeller centered in the duct and with the propeller in the upstream position, respectively. At similar rotation rates, the thrust and torque generated by the ducted propeller were less than the isolated propeller. The change in loading affects the acoustics, so once again, the measured values were used in the corresponding acoustic models. Note that the duct configuration evaluated in this study has a simple shape and a relatively large 0.5 cm gap between the propeller tip and inner duct wall. These characteristics degrade the aerodynamic performance of the system but were adequate for the acoustic evaluation.

Table 3: Measured propeller thrust and torque with the propeller centered in the duct.

RPM	BPF (Hz)	Propeller Thrust (N)	Duct Thrust (N)	Torque (Nm)
7985	399	2.93	0.34	0.07
8376	419	3.30	0.44	0.08
8989	449	3.83	0.58	0.09

Table 4: Measured propeller thrust and torque with the propeller in the upstream position.

RPM	BPF (Hz)	Propeller Thrust (N)	Duct Thrust (N)	Torque (Nm)
7997	400	2.67	0.26	0.07
8398	420	3.02	0.35	0.07
8997	450	3.48	0.45	0.08

Figure 10 compares predicted and measured sound pressure levels at the BPF for the ducted configurations. The two agree quite well, particularly at the higher rotation rates. The match in absolute levels is surprising given the underprediction observed for the isolated case. This suggests a possible issue with the thickness noise component of the source noise model, which based on Figure 7, is more dominant for the isolated configuration. Regardless, the good agreement for the ducted configuration shows that the acoustic model can accurately capture the impact of the duct on propagation and scattering. Specifically, the results show a reduction of approximately 5 dB at nearly all microphone locations when the propeller is centered in the duct relative to the upstream position. This reduction in sound pressure level is achieved even though the propeller generates more thrust in the centered position. The reduction in the level at the BPF is attributed to destructive interference between upstream and downstream radiation. When the propeller is in the upstream position, the symmetry is lost and destructive interference is reduced.
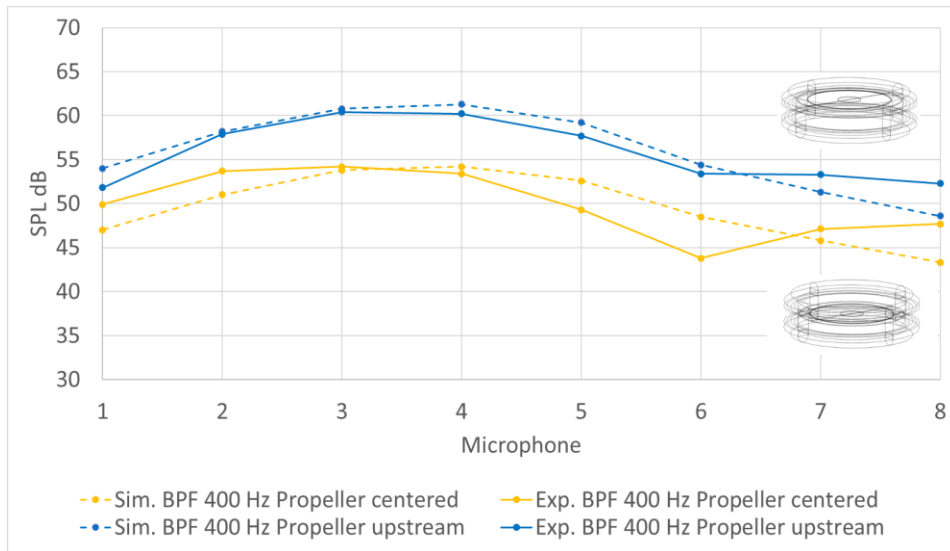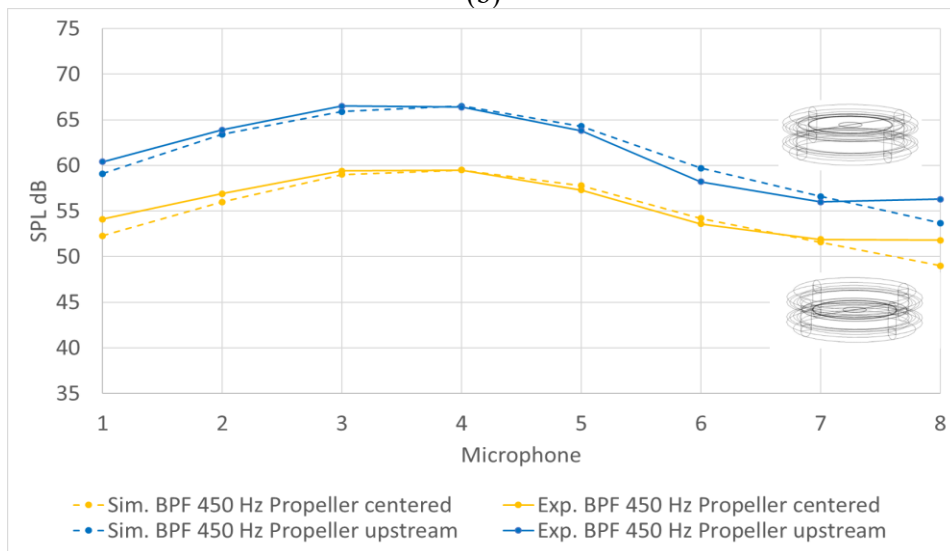
(a)
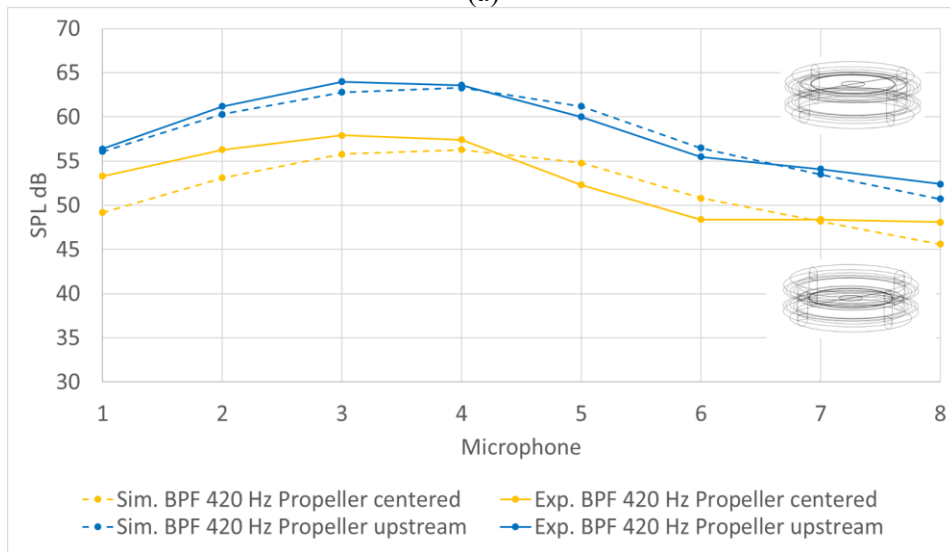
(b)

(c)

Figure 10: Simulated and measured sound pressure level (dB re. 20 μPa) for the ducted propeller at three rotation rates.

Finally, Figure 11 compares the predicted sound pressure level contours (normal to the propeller plane) at 450 Hz for the isolated propeller and the ducted configuration (with the propeller centered).

For this configuration and operating condition, the duct does not have a significant impact on the directivity but does reduce the overall levels. Again though, it is useful to keep in mind that the isolated propeller model underpredicted the levels by approximately 3 dB relative to measurements.
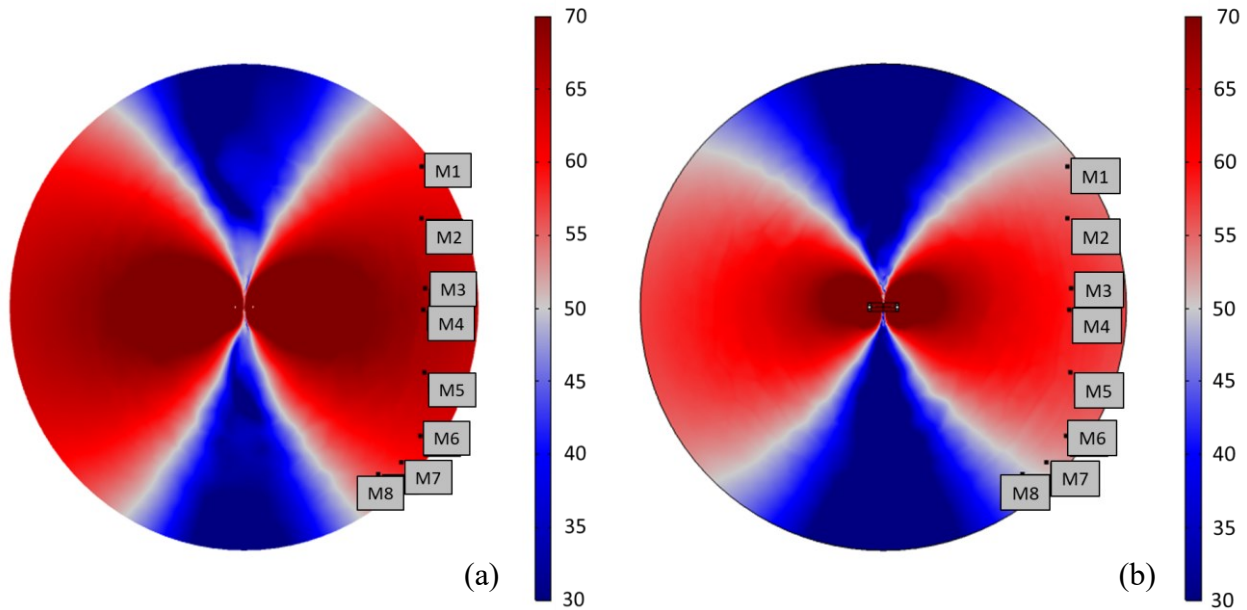

Figure 11: Predicted sound pressure level contour (dB re. 20 µPa) normal to the propeller plane for (a) the isolated propeller and (b) the centered ducted propeller at the propeller BPF of 450 Hz.

5. CONCLUSIONS

The acoustic radiation from a ducted propeller was evaluated using an acoustic finite element model. The simulation included a rigid duct and propeller source noise model that captured steady loading and thickness noise. The study demonstrates the acoustic benefit of centering the propeller axially in the duct to maximize destructive interference between upstream and downstream radiation in hover, for the geometry considered. This trend was confirmed with experiments conducted in an anechoic chamber at three propeller rotation rates.

6. ACKNOWLEDGEMENTS

7. REFERENCES

1. Sinibaldi, G. & Marino, L. Experimental analysis on the noise of propellers for small UAV. *App. Acoustics*, **74**, 79–88 (2013).

2. JanakiRam, D. S. & Scruggs, B. W. Noise and detectability characteristics of small-scale remotely piloted vehicle propellers. *J. Aircraft*, **19** (1982).

3. Serré, R., Gourdain,N., Jardin, T., Jacob M. C. & Moschetta, J-M. Towards silent micro-air vehicles: optimization of a low Reynolds number rotor in hover. *International Journal of Aeroacoustics*, **18(8)**, 690–710 (2019).

4. Zawodny, N. S., and Boyd, D. D. Jr. Investigation of Rotor-Airframe Interaction Noise Associated with Small-Scale Rotary-Wing Unmanned Aircraft Systems. *Journal of the American Helicopter Society*, **65**(012007):1–18, (2020).

5. Zawodny, N. S. and Pettingill, N. A. Acoustic Wind Tunnel Measurements of a Quadcopter in Hover and Forward Flight Conditions. In *Inter-Noise 2018*, Chicago, IL, (2018).

6. Van Treuren, K. & Wisniewski, C. Testing propeller tip modifications to reduce acoustic noise generation on a quadcopter propeller. ASME Turbo Expo, 1, *Journal of Engineering for Gas Turbines and Power* (2019).

7. Noda, R., Nakata, T., Ikeda, T., Chen, D., Yoshinaga, Y., Ishibashi, K., Rao, C. & Liu, H. Development of bio-inspired low-noise propeller for a drone. *Journal of Robotics and Mechatronics*, **30 (3)**, 337-343 (2018).

8. Halimi, A., Marinus, B. G. & Larbi, S. Analytical prediction of broadband noise from mini-RPA propellers with serrated edges. *International Journal of Aeroacoustics*, **18(4–5)**, 517–535 (2019).

9. Martin, P.B. & Boxwell, D.A. Design, analysis, and experiments on a 10-inch ducted rotor VTOL UAV. *Proceedings of AHS International Specialists' Meeting - Unmanned Rotorcraft: Design, Control and Testing*, 399-420, 2005.

10. Malgoezar, A. M. N., Vieira, A., Snellen, M., Simons, D. G. & Veldhuis, L. LM Experimental characterization of noise radiation from a ducted propeller of an unmanned aerial vehicle, *International Journal of Aeroacoustics*, **18(4–5)**, 372–391 (2019).

11. Prentice, P. R. The acoustic ring source and its application to propeller acoustics. *Proc. R. Soc. Lond. A*, **437**, 629-644 (1992).

12. Chapman, C. J. The structure of rotating sound fields. *Proc. R. Soc. Lond. A*, **440**, 257-271 (1993).

13. Garrick, I. E. & Watkins, C. E. A theoretical study of the effect of forward speed on the free – space sound-pressure field around propellers. NACA TN 3018 (1953).

14. Hanson, D. B. Helicoidal Surface Theory for Harmonic Noise of Propellers in the Far Field. *AIAA Journal*, **18(10)** (1980).

15. Hanson D.B. The influence of propeller design parameters on far field harmonic noise in forward flight. *AIAA Journal*, **18(11)** (1980).

16. Nguyen, L. C., and Kelly, J. J. A users guide for the NASA ANOPP Propeller Analysis System, NASA CR 4768 (1997).

17. Zorumski, W. Aircraft Noise Prediction Program theoretical manual, Part 1, NASA TM-93199 (1982).